



HAL
open science

Assessing the Nature of Active Sites on Nanodiamonds as Metal-Free Catalysts for the EB-to-ST Direct Dehydrogenation Using a Catalytic Approach

Lu Feng, Sajjad Ali, Chi Xu, Shuo Cao, Giulia Tuci, Giuliano Giambastiani, Cuong Pham-Huu, Yuefeng Liu

► **To cite this version:**

Lu Feng, Sajjad Ali, Chi Xu, Shuo Cao, Giulia Tuci, et al.. Assessing the Nature of Active Sites on Nanodiamonds as Metal-Free Catalysts for the EB-to-ST Direct Dehydrogenation Using a Catalytic Approach. ACS Catalysis, 2022, 12 (10), pp.6119-6131. 10.1021/acscatal.2c00825 . hal-03760604

HAL Id: hal-03760604

<https://hal.science/hal-03760604>

Submitted on 25 Aug 2022

HAL is a multi-disciplinary open access archive for the deposit and dissemination of scientific research documents, whether they are published or not. The documents may come from teaching and research institutions in France or abroad, or from public or private research centers.

L'archive ouverte pluridisciplinaire **HAL**, est destinée au dépôt et à la diffusion de documents scientifiques de niveau recherche, publiés ou non, émanant des établissements d'enseignement et de recherche français ou étrangers, des laboratoires publics ou privés.

Assessing the Nature of Active Sites on Nanodiamonds as Metal-Free Catalysts for the EB-to-ST Direct Dehydrogenation Using a Catalytic Approach

Lu Feng^{a,b,‡}, Sajjad Ali,^{c,‡} Chi Xu,^{b,d} Shuo Cao,^{b,d} Giulia Tuci,^e Giuliano Giambastiani,^{e,f,*}
Cuong Pham-Huu,^f Yuefeng Liu,^{b,*}

^a Zhang Dayu School of Chemistry, Dalian University of Technology, 116024 Dalian, China

^b Dalian National Laboratory for Clean Energy (DNL), Dalian Institute of Chemical Physics, Chinese Academy of Science, 457 Zhongshan Road, 116023 Dalian, China. Email: yuefeng.liu@dicp.ac.cn (Y. Liu)

^c Yangtze Delta Region Institute (Huzhou), University of Electronic Science and Technology of China, Huzhou 313001, China.

^d College of Chemical Engineering, Sichuan University, Chengdu 610065, China

^e Institute of Chemistry and Processes for Energy, Environment and Health (ICPEES), UMR 7515 CNRS-University of Strasbourg, 25 rue Becquerel, 67087 Strasbourg Cedex 02, France. Email: giambastiani@unistra.fr (G. Giambastiani)

^f Institute of Chemistry of OrganoMetallic Compounds, ICCOM-CNR and Consorzio INSTM, Via Madonna del Piano, 10-50019, Sesto F.no, Florence, Italy. Email: giuliano.giambastiani@iccom.cnr.it (G. Giambastiani)

[‡] These authors equally contributed to this work.

ABSTRACT

The steam- and oxygen-free alkane direct dehydrogenation (DDH) is a greener, safer and more selective alternative to oxygen co-fed conditions for the production of olefins. Carbon-based catalysts have significantly boosted this branch of catalysis providing cheaper, robust, durable and more environmentally friendly single-phase materials as valuable substitutes of a variety of alkaline- or alkaline earth-promoted transition metal oxides. In particular, nanodiamonds (NDs) rank among the most effective and selective metal-free systems investigated so far for the alkane-to-alkene conversion under either oxidative or direct dehydrogenation conditions. Although important structural/ compositional/ activity relationships for this class of sp^2/sp^3 C-hybrids have already been unveiled for the exothermic oxidative dehydrogenation (ODH) process, many issues still remain to be addressed for the more challenging oxygen-free direct dehydrogenation process. In particular, the mechanism and nature of active sites in carbon catalysts employed for the alkanes steam-free DDH still remain a controversial matter of debate because of the lack of studies under harsher operative conditions typically required by this endothermic process. Here, we report on the chemico-physical and morphological properties of diamond samples before and after their use as catalysts in the model ethylbenzene-to-styrene dehydrogenation using oxygen- and oxygen-free conditions. The combination of the catalytic outcomes with the extensive characterization of these metal-free systems, led us to speculate on the nature of oxidized carbons as catalytically active sites in the DDH process. DFT calculations have finally been used to corroborate our hypotheses, providing support to the role of ortho-quinone (oQ) groups at the edge of cubic- sp^3 NDs as the oxidized carbon source (active sites) for DDH.

KEYWORDS: Nanodiamonds (NDs); EB-to-ST steam-free direct dehydrogenation; carbonyl moieties on sp^3 -cubic NDs; thermal C-OH decomposition to C=O

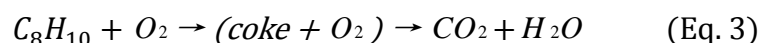
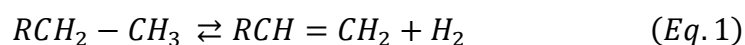
1. INTRODUCTION

Properties and reactivity of unsaturated organic compounds make them highly attractive building blocks in many chemical fields. From a practical viewpoint, they are essentially produced by dehydrogenation of their saturated counterparts.¹⁻³ Styrene (ST), a colorless liquid derived from ethylbenzene (EB) is a fundamental industrial component for the production of several synthetic rubbers, resins, and plastics with a global market driven by the production of polystyrene. The latter, a thermoplastic resin that can be easily processed, holds a priority position in packaging industry.⁴ Nowadays, global Styrene (ST) demand is approaching 16.5 million tons per year with an estimated annual growth rate (CAGR) of 3.85 %.⁵ ST production involves a highly energy demanding process, associated with large carbon footprint, in a chemical transformation typically carried out by a K-promoted iron oxide catalyst ($\text{K-Fe}_2\text{O}_3$ or K-Fe) at temperatures comprised between 580 and 630 °C.⁶ Despite of heavy deactivation phenomena of K-Fe-based systems due to the rapid passivation/coking of their metal active sites and the potential environmental impact associated to the leaching of metal nano-objects, they remain the most studied and industrially used catalysts for the process.

Recent years have witnessed a growing interest of the catalysis community towards the use of single-phase catalysts based on carbon nanomaterials in the form of pure C-networks or light-heterodoped matrices. The control of their surface chemical properties in terms of distinctive functional groups available, defective sites or light hetero-elements along with their ultimate morphology have unveiled the potentialities of these metal-free systems within a variety of catalytic applications.⁷⁻¹⁰ They have successfully been scrutinized as valuable

catalytic systems for a number of industrially relevant oxidation¹¹⁻²² and reduction²³⁻³¹ processes, including other challenging catalytic transformations.³²⁻³⁵ Their high thermal stability, good electrical conductivity, porosity and tunable surface composition have boosted their exploitation in catalysis, often pointing out their superior activity and stability compared to traditional metal or metal oxide-based systems. On the other hand, their complex structure and surface composition have often limited the comprehension of the underpinning reaction mechanisms and thus the identification of the nature of active sites involved in a given catalytic process.

As far as the alkane dehydrogenation catalysis is concerned, selected nanocarbon structures have shown excellent catalytic outcomes along with unique “anticoking” properties¹⁹ in the endothermic EB direct dehydrogenation (DDH) under steam- and oxygen-free conditions (Eq. 1).^{15, 36-40} Exothermic oxidative dehydrogenation (ODH) conditions make the process more attractive from a thermodynamic viewpoint, ultimately allowing the process to take place under milder temperature conditions (Eq. 2), but with a generally lower selectivity due to the formation of CO₂ as side-product (Eq. 3).⁴¹



Moreover, recent studies have unveiled the importance of an oxidative environment for the generation of selected surface oxygenated functional groups suitable to act as redox-active sites for the dehydrogenation process to occur.^{36, 42-47} Qi *et al.* reported on the identification and quantification of active sites in nanocarbon catalysts employed in the EB oxidative

dehydrogenation by a chemical titration method.⁴³⁻⁴⁴ Their pioneering work demonstrated the role of carbonyl fragments as Lewis bases for the C-H bond activation of EB followed by the catalyst active sites regeneration under the oxidative environment. In more recent years, other papers have contributed to consolidate the role of carbonyl fragments (typically quinone units) in nanocarbon-based materials engaged as metal-free catalysts for the alkane dehydrogenation reaction under oxidative conditions.⁴⁸⁻⁵² On the other hand, the mechanism and nature of active sites in carbon catalysts employed for the steam-free DDH of alkanes still remain controversial, also because of the lack of studies under harsher operative conditions typically required by this endothermic process. In principle, the reaction mechanism might imply the occurrence of unconventional redox paths involving again quinone groups followed by the thermal regeneration of their hydroxyl-counterparts under severe operative conditions.^{36, 53-55} Other reports also refer to a more general and not-specified action of C-defects/vacancies in the alkane C-H bond activation.²¹ As far as the involvement of surface carbonyl groups in DDH is concerned, it is generally believed that their cyclic regeneration path under an oxygen-free atmosphere is ensured by the thermal decomposition of C-OH groups into C=O with evolution of molecular hydrogen, a thermodynamically favorable process at high operative temperatures.^{36, 53-55}

This contribution offers an original hint to the comprehension of the most likely active groups involved in DDH through a rational analysis of the chemico-physical and morphological characterization of nanodiamond (ND) samples after undergoing EB (ethylbenzene) dehydrogenation catalysis to ST (styrene) using oxidative (ODH) and/or steam-free direct dehydrogenation (DDH) conditions. The combination of the catalytic

outcomes with an extensive characterization of these metal-free systems (before and after catalysis) led us to speculate on the nature of the oxidized carbons as catalytically active sites throughout the DDH process.⁵⁶ First-principles calculations have finally corroborated our speculations, providing additional support to our mechanistic hypothesis. In particular, in silico studies have pointed out on the feasibility nature of the oxidant-free regeneration mechanism of the active functional groups involved in DDH.⁵⁷

NDs have been selected because of the important structural/activity relationships that this class of sp^2/sp^3 C-hybrids has deeply contributed to elucidate in carbocatalysis.⁵⁸ Moreover, they certainly rank among the most effective and selective metal-free systems reported so far in the literature for the alkane-to-alkene conversion under either ODH^{41, 59-62} or oxygen and steam-free DDH^{36, 63} conditions. To this aim, purified ND and their thermally annealed (1100 °C) counterparts (ND₁₁₀₀) featured by a higher degree of graphitization of their outer sphere were prepared and tested in dehydrogenation catalysis.

2. Experimental section

2.1 *Materials and methods*

Nanodiamonds (NDs) obtained by detonation explosive method were purchased from Beijing Grish Hitech China in the form of microcrystalline powders and were purified from detonation soot upon treatment with HCl 12M prior any use.⁶⁴ The as-produced NDs are typically made of sp^3 -hybridized nanocrystals (5 ± 2 nm) with irregular morphology, high surface/volume ratio and contain surface hydrogen and oxygen atoms. Their thermal annealing at high temperatures (> 900 °C) is known to largely reduce heteroelements

concentration from the nanocrystals surface while promoting the collapse and transition of C_{sp3} into C_{sp2} . Accordingly, a portion of purified NDs was then calcined in a furnace at 1100 °C for 3 h under a dynamic Ar atmosphere (80 mL min⁻¹). The as treated solid portion was then cooled down to room temperature, collected and stored at ambient conditions. The latter was conventionally named as ND₁₁₀₀ (**2**) to be distinguished from the simply acid-treated samples (NDs, **1**). Unless otherwise stated, all other reagents, solvents and gases were used as received from the respective providers. The X-ray diffraction (XRD) patterns were collected from 5 to 90° using X'pert-Pro diffractometer (PAN Analytical, Holland) with monochromatic Cu K radiation ($\lambda = 0.1542$ nm, accelerating voltage 40 kV, applied current 40 mA). High-resolution TEM images were operated on Titan Themis G3 ETEM (Thermo Scientific) equipped with a spherical-aberration corrector (CEOS GmbH) for parallel imaging at 300 kV and a resolution higher than 1.0 Å. The EELS analyses were performed on STEM model on Hitachi HF5000 microscope with probe corrector at 200 kV cold-field emission gun. The energy resolution for the EELS system was higher than 60 meV, which was determined from full-width at half-maximum (FWHM) of the zero-loss peak.

UV-Raman spectroscopy was performed on powder samples using a Horiba LabRam HR Raman spectrometer. The excitation wavelength used for each analysis was 325 nm with a power of 0.2 mW.

X-ray adsorption spectra (XAS) were measured at the soft X-ray Magnetic Circular Dichroism Endstation (XMCD) beamline of national synchrotron radiation laboratory (NSRL, Hefei, China). The powdered sample was packed onto a conductive adhesive without any further treatment. The C K-edge, N K-edge and O K-edge X-ray absorption near edge

structure (XANES) spectra were collected under ultra-high vacuum (10^{-8} Pa).

X-ray photoelectron spectroscopy (XPS) measurements were carried out on a Thermo Fisher ESCALAB 250Xi spectrometer equipped with monochromatic Al K α ($h\nu = 1486.6$ eV, 15 kV, 10.8 mA). The binding energies were calibrated on the carbon C1s peak at BE = 284.6 eV (accuracy within ± 0.1 eV).

Temperature-programmed desorption (TPD) experiments were carried out using a QMD mass spectrometer. In a typical experiment, ≈ 50 mg of the sample were loaded in the reactor and purged for 30 min at room temperature under an He stream (40 mL min^{-1}). TPD measurements were carried out in the 100-900 °C temperature range using a heating rate ramp of $10 \text{ }^\circ\text{C min}^{-1}$ while keeping constant the inert gas flow throughout the whole analysis. For each sample, the $m/z = 44$ (CO_2) and $m/z = 28$ (CO) were registered in the fully swept temperature range. EPR measurements were carried out on a Bruker A200 electron paramagnetic resonance instrument.

2.2 *EB-to-ST direct (DDH) and oxidative (ODH) dehydrogenation trials*

EB-to-ST dehydrogenation was operated in a continuous flow over a fixed-bed quartz reactor ($\varnothing_{\text{id}} = 10$ mm; tube length = 400 mm) loaded with 150 mg of catalyst. The catalytic dehydrogenation process was then performed under either oxygen (ODH) or oxygen-free (DDH) conditions. When dehydrogenation was operated under oxygen atmosphere (ODH), the reactor was heated up to 450 °C with a temperature ramp of $10 \text{ }^\circ\text{C min}^{-1}$ while keeping the catalyst under a constant stream of He (30 mL min^{-1}). Afterwards, the reactor was left to stabilize to the target temperature for 30 min under a pure He flow before purging the system with a 2.9 vol.% of O_2 in He (30 mL min^{-1}). The latter stream was then passed through a glass

evaporator filled with EB constantly maintained at the temperature of 40 °C. Accordingly, an EB fraction of 2.8 vol.% was passed through the catalytic bed (EB partial pressure = 2.9 kPa). ND-ODH and ND₁₁₀₀-ODH acronyms were conventionally used to identify pristine ND and ND₁₁₀₀ catalysts after undergoing ODH conditions, respectively.

For the oxygen- and steam-free dehydrogenation catalysis (DDH), the reactor was heated up to 550 °C and maintained at the target temperature for 30 min under a pure stream of He (30 mL min⁻¹). Afterwards, the He stream was simply passed through the glass evaporator containing EB at the temperature of 40 °C.

Whatever the dehydrogenation conditions used, a qualitative and quantitative analysis of reactants and products was determined in real time at the reactor outlet [EB, O₂, ST, toluene (tol), benzene (bz) and CO_x (x = 1, 2)] using an Agilent 7820 A gas chromatography equipped with a flame ionization detector (HP-INNOWAX column) and a thermal conductivity detector. To avoid any adventitious condensation of organic components and water during dehydrogenation reactions (ODH and DDH), all pipe lines were constantly maintained at 120 °C by means of external heating tapes. Whatever the catalytic systems at work, EB conversion (X_{EB}) and ST selectivity (S_{ST}) were conventionally assumed as those at the steady-state conditions (namely, after 15 h on stream).

Ethylbenzene conversion (X_{EB}), styrene selectivity (S_{ST}) and styrene yield (Y_{ST}) were evaluated using equations 4 - 6:

$$X_{EB} = \frac{F_0 C_{EB,in.} - F C_{EB,out.}}{F_0 C_{EB,in.}} \times 100 (\%) \quad (Eq. 4)$$

$$S_{ST} = \frac{C_{ST,out.}}{C_{ST,out.} + C_{tol,out.} + C_{bz,out.} + C_{CO,out.} + C_{CO_2,out.}} \times 100 \text{ (\%)} \quad (Eq. 5)$$

$$Y_{ST} = X_{EB} \times S_{ST} \quad (Eq. 6)$$

where F and F_0 are the flow rates of the reactor outlet (*out*) and inlet (*in*), respectively, while C_{EB} , C_{ST} , C_{tol} , C_{bz} and CO_x ($x = 1, 2$) correspond to the concentration of ethylbenzene, styrene, toluene, benzene and carbon oxides. The carbon balances amounted to around 100% in all investigations.

2.3 DFT modelling

The *in silico* study was carried out through spin-polarized DFT using generalized gradient approximation (GGA) and the Perdew-Burke-Ernzerhof (PBE)⁶⁵ functional for the exchange-correlation potentials as implemented in the Vienna ab initio simulation package (VASP).⁶⁶⁻⁶⁸ A $3 \times 3 \times 3$ and $9 \times 9 \times 1$ k-points mesh with 520 eV energy cutoff were used for ND and graphene structure relaxation respectively. The empirical correction in Grimme's method (DFT+D3) was adopted to describe the van der Waals interactions.⁶⁹ The total energy was converged to an accuracy of 1×10^{-5} eV to obtain accurate forces, and a force tolerance of -0.02 eV/Å was applied in the structure optimization. Here we considered different oxidized carbons on sp^2 , sp^2/sp^3 and sp^3 networks for DDH and the regeneration of the catalytically active functional groups. To model the hybrid sp^2/sp^3 cluster and the cubic sp^3 ND, a $30 \times 30 \times 30$ Å³ cubic cell (octahedral), and a $23 \times 23 \times 23$ Å³ for the x, y, z dimensions were used respectively. The reaction pathways and energy barriers for the DDH reaction were calculated using the climbing image nudged elastic band (CI-NEB) method.⁷⁰

3. Results and Discussion

This study focuses on the surface properties of a series of modified nanodiamonds and their ability to act as metal-free systems in the challenging EB-to-ST catalytic process. Our approach moved from the analysis of the catalytic performance of pristine or thermally annealed diamonds under oxygen- (ODH) or oxygen-free and steam-free (DDH) conditions. A complete physico-chemical and morphological characterization of all materials before and after catalysis was used to assess the role of surface graphitization and chemical composition of diamond samples with respect to their ability to perform the DDH process.

3.1 Catalytic tests of ND samples under ODH and DDH conditions

In a first catalytic trial, pristine ND and ND₁₁₀₀ samples were tested as catalysts for the EB-to-ST oxidative dehydrogenation (ODH) at 450 °C. As Figure 1 shows, after an initial induction period, the catalysts activity grew asymptotically and stabilized to 45 and 55 % for ND and ND₁₁₀₀, after 30 and 20 h time-on-stream (TOS), respectively. Whatever the catalytic system at work, styrene selectivity (S_{ST}) laid almost constantly between 88 and 92%. In spite of similar ethylbenzene conversion trends (X_{EB}), the higher performance measured with ND₁₁₀₀ prompted us to speculate on the origin of the superior ODH activity on this thermally annealed sp^2/sp^3 hybrid. According to previous literature reports,^{36, 42-52} the increasing X_{EB} measured with both catalytic systems under ODH conditions was consistent with the *in-situ* generation of newly oxidized C-sites. However, different X_{EB} performance measured for the two catalysts reflected the different aptitude of the two C-networks to generate oxidized

carbons (*i.e.* carbonyl/quinone functionalities) suitable for the process to occur.

When the two systems reached a constant plateau, oxygen was deliberately removed from the gaseous stream and the reactor temperature was increased up to 550 °C to continue the dehydrogenation process under oxygen-free (DDH) conditions. After a short equilibration time, X_{EB} stabilized to 5 and 9% for ND and ND₁₁₀₀, respectively, whereas S_{ST} slightly grew up to 97% on both systems. We were aware about the reasons of the different catalytic performance under DDH conditions as well as the higher temperature required by this endothermic process to take place. The removal of oxygen from the reagents stream stopped the redox catalytic loop on both catalytic systems and X_{EB} collapsed suddenly. If its gradual decrease in the first hours under DDH conditions was still associated to a progressive consumption/reduction of residual carbonyl moieties at the diamonds surfaces, its fast and constant stabilization to lower conversion values was likely due to the ability of these C-networks to foster the EB-to-ST conversion through different mechanistic paths whose nature still remains matter of debate. Noteworthy, the comparative DDH study on ND and ND₁₁₀₀ samples not previously submitted to ODH conditions (blue rhombuses in Figure 1A' and 1B'), showed the superior catalytic performance of these pristine samples that exhibited X_{EB} values up two-times higher than those recorded on ND-ODH and ND₁₁₀₀-ODH materials (red spheres in Figure 1A' and 1B'), respectively.

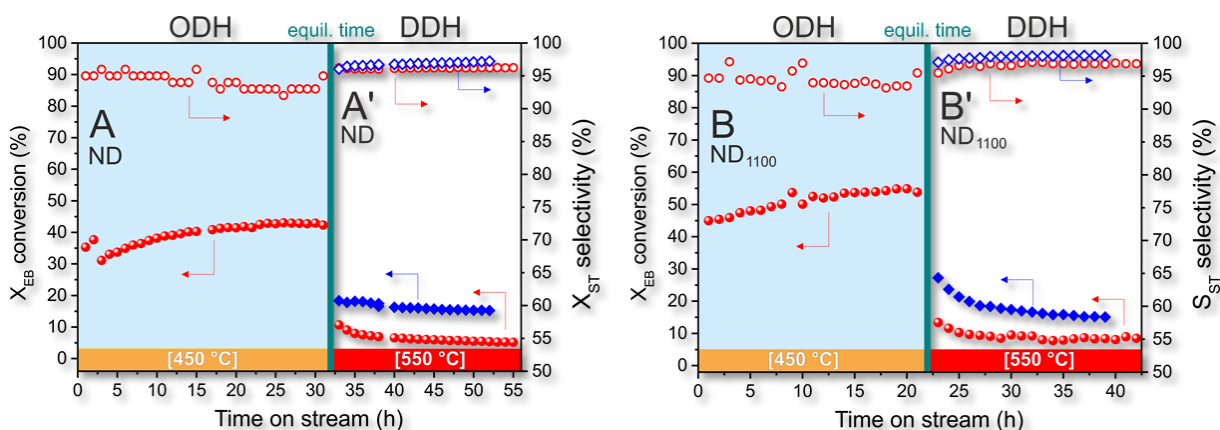


Figure 1. Catalytic performance of ND (A, A') and ND₁₁₀₀ (B, B') as catalysts in the EB-to-ST ODH (A and B) and DDH (A' and B'), respectively. Blue rhombuses (\blacklozenge : X_{EB} ; \blacklozenge : S_{ST}) in A' and B' refer to the catalytic behavior of pristine ND and ND₁₁₀₀ directly under DDH conditions. For a better comparison, the start time for the DDH reaction of the pristine catalysts (ND, ND₁₁₀₀) has been shifted to coincide with the ODH-treated counterparts. ODH conditions: 150 mg cat., O₂: 2.9 vol.%, reaction temperature: 450 °C, EB : O₂ = 1 : 1. DDH conditions: 150 mg cat. reaction temperature: 550 °C, EB : He = 2.8 mLmin⁻¹: 27.2 mLmin⁻¹)

Such a comparative analysis unveiled that ODH conditions affected detrimentally the catalysts surface properties, reducing their performance in catalysis when they were operated under the more challenging oxygen-free dehydrogenation (DDH) conditions. On the other hand, DDH conditions did not change appreciably the surface properties of catalytic materials, particularly with respect to those surface functional groups engaged under ODH conditions. Indeed, when O₂ was restored in the reagents stream, ND activity was fully and suddenly recovered and the catalytic system stabilized fast to the expected X_{EB} and S_{ST} values previously recorded at the steady-state conditions (Figure S1).

A complete characterization of pristine and ODH-treated nanodiamonds has been accomplished to shed light on the nature of chemical/morphological modifications incurring the diamonds throughout each thermal and/or catalytic step they underwent. To this regard, ND (1) and ND₁₁₀₀ (2) recovered after ODH were conventionally indicated as follows: ND-

ODH (**3**) and ND₁₁₀₀-ODH (**4**), respectively.

3.2 Fresh and used catalysts characterization

The electron paramagnetic resonance (EPR) was initially selected as a non-destructive tool for the assessment of the role played by each thermal and/or catalytic treatment on the diamonds electron properties. This technique has already been used to assess the presence of paramagnetic centers (unpaired electrons) in defective C-solids, carbon dangling bonds and light-heterodoped constraint carbons.^{58, 71} With **1-4**, EPR analysis gave single lines at $g = 2.002$ with no visible fine or hyperfine structures (Figure 2A). A reduction of paramagnetic centers was measured in the material annealed at 1100 °C only (**1** → **2**; Figure 2A) while negligible changes were detected in the intensity of EPR signals of all ODH-treated samples from this series (**1** → **3** and **2** → **4**; Figure 2A).

Although a reduction of paramagnetic sites density in amorphous C-networks has already been documented for lower annealing temperature values (*i.e.* 300 °C),⁷²⁻⁷³ only harsher thermal conditions seemed to affect appreciably this property in nanodiamonds. Therefore, only high-temperature annealing was found to affect the whole materials structure appreciably by initiating a bulk restructuring of the diamond defective sites into more stable and inert structures containing a reduced number of unpaired electrons.⁵⁸

Electron energy loss spectroscopy (EELS) was then selected to assess the degree of graphitization at the diamonds outer sphere as a result of the thermal and/or chemo-thermal treatments (ODH) they were submitted to.

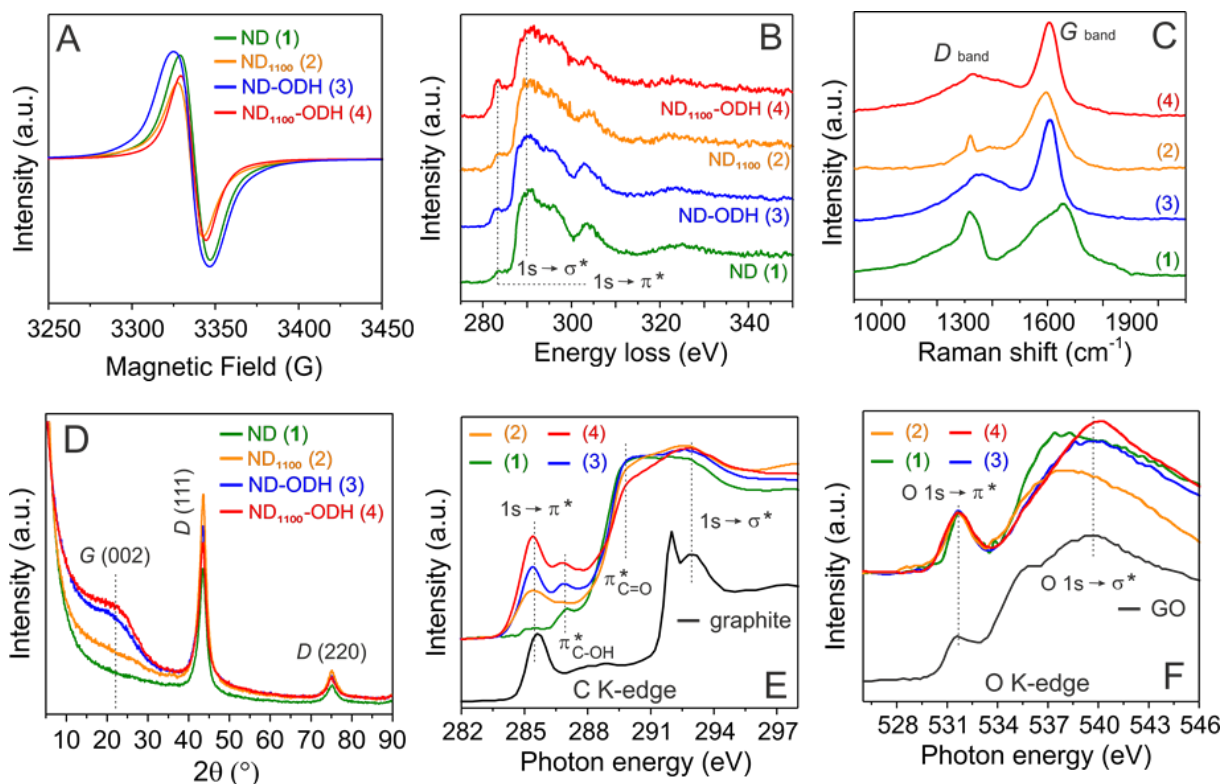


Figure 2. A) EPR spectra of samples **1-4** at comparison. EELS (B), Raman (C) and XRD (D) spectra of samples **1-4** at comparison. E) XANES spectra of samples **1-4** at the C K-edge along with that of a benchmark graphite sample, added for the sake of comparison. F) XANES spectra of samples **1-4** at the O K-edge along with that of a benchmark graphene-oxide (GO) sample, added for the sake of comparison.

As Figure 2B shows, all high-energy samples' profiles at the C K-edge presented characteristic and prominent components at 290.0 eV whose origin was attributed to the $1s \rightarrow \sigma^*$ electrons excitation on sp^3 -hybridized C-cores of the crystalline diamonds. A minor shoulder, due to the $1s \rightarrow \pi^*$ electrons transition on C_{sp^2} networks was equally observed on the normalized EEL spectra at lower energy values (≈ 283.9 eV).⁷⁴ This latter indicated the presence of a certain extent of sp^2 -hybridized carbon in all samples, including pristine ND.⁷⁵⁻⁷⁶ Noteworthy, ODH conditions were found to increase appreciably the peak intensity at 283.9 eV on both samples. Despite the lower temperatures of ODH conditions respect to those employed in the annealing phase, a phase-transition (from cubic diamond to sp^2 -graphitized

networks) in diamond powders cannot be definitively ruled out because of the small size and large surface-area-to-volume ratio of nanocrystallites. However, catalyst “coking” and the generation of newly formed C-deposits in the form of sp^2 -hybridized networks at the diamonds outer surface is another option to consider for materials exposed to ODH conditions for prolonged times. It seems reasonable to admit that newly formed C-deposits were homoepitaxially grown on sp^2 -graphitized portions of diamonds **1** and **3** during the catalytic oxidative treatment. Indeed, as Figure 2B shows, the higher the graphitization degree of the starting C-network the higher the peak intensity growth associated to sp^2 -hibridized carbons on ODH treated samples (Figure 2B, **1** vs. **3** and **2** vs. **4**). Overall, ODH conditions were found to alter significantly the surface properties of the C-based nano-objects. Raman spectroscopy (Figure 2C) is highly sensitive to different types of carbon bonding at the surface of diamonds and data recorded on all samples from this series were in good accord with EEL outcomes. Pristine NDs (**1**) showed a defined diamond peak (D) centered around 1330 cm^{-1} along with a broadener peak at 1650 cm^{-1} resulting from the superimposition of OH bending ($\approx 1640\text{ cm}^{-1}$), C=O stretching vibrations ($\approx 1740\text{ cm}^{-1}$) and the graphitic (G) band centered at 1590 cm^{-1} corresponding to the first-order scattering of tangential C_{sp^2} stretching (E_{2g}) mode.⁷⁷ Spectra recorded on annealed and ODH-treated diamonds (Figure 2C, **1** to **3** and **2** to **4**) showed a sharp narrowing of the latter peak which was shifted closer to the G-band (red shift), consistent with an increase of C_{sp^2} graphitic structures.⁷⁸⁻⁷⁹ The G-modes of the treated diamonds (**2-4**) retained relatively broad shapes due to the large variation in the materials bond lengths along with a large background from amorphous carbon around 1520 cm^{-1} .⁸⁰ IR Spectroscopy (Figure S2) further confirms the presence of carbonyl/quinones groups in

pristine NDs and in their counterparts after ODH. In particular, a strong band at 1774 cm^{-1} is observed in sample **1** while the same signal is red shifted to 1743 cm^{-1} because of the increasing of C_{sp^2}/C_{sp^3} ratio in ND-ODH (**3**).⁸¹⁻⁸²

The XRD patterns recorded on samples **2-4** were also consistent with an appreciable increase in the graphitization degree on all cubic structures. Figure 2D shows distinctive features of pristine and treated nanodiamonds which hold two characteristic diffraction peaks at $2\theta = 43.8^\circ$ and 75.2° corresponding to the (111) and (220) cubic diamond planes. Noteworthy, all thermal (**2**) and chemo-thermally (**3,4**) treated samples presented an additional and broad shoulder at $2\theta \approx 22^\circ$ corresponding to (0 0 2) crystal graphite planes.⁸³ All diffraction peaks were obviously broadened due to the very small crystallite size. However, the growth of the broad (002) component in samples **2-4** indicated unambiguously that upon materials treatment the contribution from the graphitic C_{sp^2} -structures increased.⁷⁹ A strong background in the lower angle region ($< 15^\circ$) of all spectra finally suggested the presence of amorphous material in nanodiamond powders.⁸⁴

To get additional details on the surface properties of diamonds before and after ODH conditions and to add fundamental tiles to the complex puzzle of the structure/composition/reactivity relationships of these samples in catalysis, we studied the X-ray absorption near-edge structure (XANES) of all materials. XANES encodes detailed information on the local chemical environment of the absorbent atoms in the samples. Therefore, C K-edge and O K-edge spectra recorded on **1-4** were used to investigate the evolution of the composition of each sample after their exposure to thermal and/or thermo-chemical treatments. This technique provided useful information on the degree of bond

hybridization in mixed C_{sp2}/C_{sp3} networks, the specific bonding configurations of foreign functional groups and the degree of alignment of graphitic crystal structures.⁸⁵ As far as C K-edge XANES spectra of all diamonds are concerned, Figure 2E shows their normalized profiles along with that of the model graphite for the sake of comparison (black curve). All spectra displayed two distinctive components at 285.5 eV and 292.8 eV, which corresponded to the transitions from C 1s core level to unoccupied π^* and σ^* states, respectively.⁸⁶ The π^* -feature is typical of out-of-plane C=C bonds or C_{sp2} from graphitic networks while the σ^* -transition typically accounts for C-C bonds.⁸⁷ More pronounced C 1s $\rightarrow \pi^*$ transitions in **2-4** accounted for the growth of sp^2 -hybridized structures in all treated diamonds. From a careful analysis of these components, we came across similar conclusions to those outlined above respect to the role of thermal annealing (**1** vs. **2**) and ODH-treatment (**1** vs. **3** and **2** vs. **4**) in the graphitization process on these C-hybrids. Wider features in the 286-289 eV range were typically ascribed to C-atoms bound to oxygen and hydrogen. Although their specific attribution remains somehow controversial,⁸⁸ they could be reasonably assigned to the following transitions: at ≈ 286.7 eV to electronic transitions from the C 1s core to π^* states of C-OH bonds; at ≈ 288.0 eV to π^* (C-O-C) and at ≈ 288.7 eV to π^* (C=O) of carboxylic fragments.⁸⁷ A large part of these components was overhung from a wide and intense background imposed by σ^* edge of C-H bonds in nanodiamond structures.⁸⁹ Accordingly, ODH treatment was found to increase hydroxyl moieties while contributing to extend the graphitization degree of the hybrids. As already noticed from EEL spectroscopy (Figure 2B), the effect of the ODH conditions on the pre-annealed **2** was more relevant than that on pristine **1**. This was demonstrated by the more appreciable increase of C 1s $\rightarrow \pi^*$ transition

and decrease of the $\sigma^*_{\text{C-H}}$ intensity in **4**.

Although any other direct conclusions remain speculative, these characterization data combined with the catalytic results lead to the conclusion that pre-annealing and exposure of nanodiamonds to ODH conditions promoted the phase transition (from cubic diamonds to graphite structures) and the epitaxial growth of new C-deposits on sp^2 -graphitized portions of diamonds, respectively. At the same time, C_{sp^2} -graphitized networks facilitated the generation of redox active C=O moieties for EB-to-ST dehydrogenation under ODH conditions while reducing (somehow) the C-based catalyst aptitude to perform the process under DDH conditions (Figure 1A' and 1B').

The O K-edge normalized spectra (Figure 2F) consisted of a pre-edge feature (sharp peak at ≈ 532 eV) and a broad post-edge component centered at ≈ 540 eV. While the first sharp peak was attributed to the transition from O 1s core level electrons to π^* C=O states derived from carboxylic acid and ketones, the broader and poorly resolved post-edge peak accounted for the transition from core shell electrons (O 1s) to the anti-bonding σ^* molecular orbital of several oxidized functions such as C-OH (≈ 537.5 eV), C-O and C=O (≈ 542.4 eV).⁹⁰⁻⁹¹ Although differences among these oxidized functionalities lie on the intensity and position of both pre-edge and post-edge peaks, their coexistence on the same sample makes hard any extensive discussion on the nature and relative abundance of these oxidized carbon.⁹² Anyway, the comparative analysis of the normalized O K-edge profiles in Figure 2F can be used to speculate on some distinctive properties among the differently treated samples. As expected, the shoulder at ≈ 537.5 eV in **1**, mainly attributed to aliphatic hydroxyl groups is deeply reduced in the annealed diamonds (Figure 2F, **1** vs. **2**).⁹² The more intense peak components at

higher energy value ($\approx 538\text{--}544$ eV) well match with the prevalence of carbonyl-type functional groups in the ODH treated materials **3** and **4**.⁹² At the same time, the lower intensity of this broad peak in **3** indirectly confirms the higher aptitude of the pre-annealed sample (ND₁₁₀₀, **2**) to generate during ODH conditions a larger extent of redox-active C_{sp2}=O functionalities on its more graphitized network.

The XPS analysis of the samples at their C 1s and O 1s core levels have been recorded to provide additional evidences of the effect of thermal annealing and/or ODH conditions on the materials phase composition and chemical environment at their outer surfaces. High-resolution C 1s and O 1s XPS spectra of samples **1-4** along with the relative Gaussian-Lorentzian (80% Gaussian and 20% Lorentzian) fittings were shown in Figure 3. C 1s peaks of all samples were conveniently fitted by four distinct components attributed (from lower to higher BEs) to C_{sp2}, C_{sp3}-hybridized networks, oxygen-bonded and carbon-oxygen double bonds moieties, respectively. Some peaks shifting to higher BEs in all samples were caused by the electrostatic charging of the samples during analysis as a result of their low conductivity and insufficient compensation by the internal flood gun.⁹³ Carbon-oxygen bonds were present in all pristine and treated samples as witnessed by the appearance of a clear O 1s peak in their samples survey spectra (Figure S3). Pristine NDs (**1**) exhibited a relatively wide peak fitted with two main components at 286.3 and 287.5 eV ascribed to C_{sp3} and carbon-oxygen bonds, together with two additional shoulders at lower (≈ 285.0 eV) and higher BEs (≈ 288.5 eV) ascribed to C_{sp2} and carbon-oxygen double bonds, respectively (Figure 3A, bottom side).⁹⁴⁻⁹⁶ Three more intense components with an appreciable increase of that due to sp²-hybridized carbons were observed in the annealed sample **2** (Figure 3B, bottom side) as a

result of the multi-graphite shell structure formed under the high temperature material treatment.

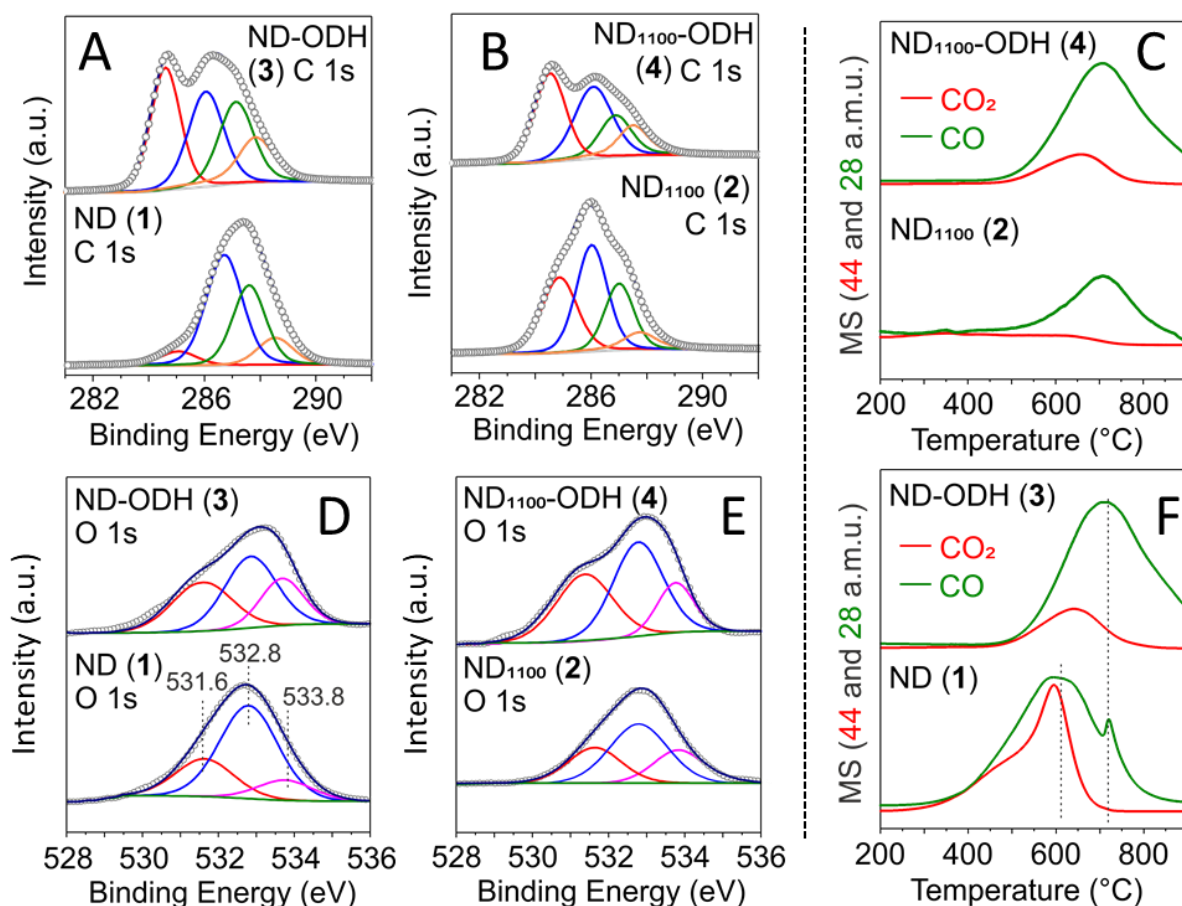


Figure 3. High resolution XPS C 1s (A-B) and O 1s (D-E) core level regions of **1** vs. **3** and **2** vs. **4**. TPD profiles of **2** vs. **4** (C) and **1** vs. **3** (F) recorded under He atmosphere with a heating rate of 10 °C min⁻¹. Green (—) and red (—) lines refer to CO, $m/z = 28$ and CO₂, $m/z = 44$, respectively.

Both ODH-treated samples exhibited four distinct components with the one dealing with C_{sp2} domain and that at higher BEs attributed to carbon-oxygen double bonds appearing appreciably more intense [Figure 3A (**1** vs. **3**) and Figure 3B (**2** vs. **4**)].

Seen from the O 1s core level spectra, all peaks were conveniently fitted with three distinctive components: those at binding energies of 531.6 and 532.8 eV were conventionally assigned to carbonyl (C=O) and carboxyl (COOH) groups, respectively,⁹⁷ whereas that at

higher energy values (533.8 eV) was attributed to hydroxy (-OH) and ether (O-C-O) fragments.⁹⁸ Remarkably, the oxygen at.% estimated by XPS analysis was found to increase of about 16 % and 150 % on the ODH-treated samples **3** and **4**, respectively (Table 1, entry **1** vs. **2** and **3** vs. **4**). As expected, a higher degree of graphitization in ODH-treated diamonds (**2** vs. **1**) translates into a higher percentage of oxidized carbons (C=O) available at the materials outer surface upon its exposure to an oxidant environment, and potentially suitable to promote ODH. Table 1 reports the O at.% in each sample along with the probability of each O-containing functionality estimated by XPS analysis. As Figure 3D,E and Table 1 show, ODH conditions increased the component at 531.6 eV (C=O) of ≈ 90 % on **3** and ≈ 225 % on **4**, respectively (Table 1, C=O %, **1** vs. **3** and **2** vs. **4**).

Table 1. Deconvolution of O 1s XPS spectra of samples **1-4**.

Entry	Sample	O cont. at.% ^a	Components of O 1s peaks (%) ^b			C=O cont. (at.%)
			Carbonyl (C=O)	Carboxylic (CO ₂ H)	Hydroxyl/Ethers -OH; C-O-C	
1	ND (1)	8.9	21.3	66.3	12.4	1.9
2	ND-ODH (3)	10.3	35.0	45.6	19.4	3.6
3	ND ₁₁₀₀ (2)	4.3	27.9	45.1	27.0	1.2
4	ND ₁₁₀₀ -ODH (4)	10.7	36.4	44.9	18.7	3.9

^a Determined from XPS analysis. ^b Determined according to the Gaussian-Lorentzian fittings of the high resolution XPS at O 1s core region.

It is known that total amount of CO and CO₂ decomposition products from temperature-programmed decomposition (TPD) analyses of C-based samples can provide additional information on the identity of the nature of oxygenated-surface groups.⁹⁹⁻¹⁰⁰ While CO₂ evolution is conventionally ascribed to carboxyl-type groups, CO preferentially originates from the decomposition of carbonyl/quinones, phenolic and ether-type functionalities. As TPD curves recorded under He-atmosphere show (Figure 3C, F), CO and CO₂ desorption start

almost at the same temperature values and curves intensity qualitatively account for diamonds surface compositions in excellent accord with the conclusions outlined from XPS analyses. In particular, the sample annealing was found to deeply reduce all O-containing surface groups (Figure 3F; ND **(1)** vs. Figure 3C, ND₁₁₀₀ **(2)**) while ODH conditions largely contributed to the growth of the carbonyl population. From a careful analysis of all these normalized curves, it can be inferred again that the higher the C-network graphitization degree, the higher the population of carbonyl functionalities potentially engaged as redox-active groups in ODH (Figure 3F vs. 3C; MS 28 a.m.u.). It should also be noticed that CO profiles of ODH-treated samples present a maximum slightly shifted to higher temperature values respect to that of pristine ND sample **1**. While a maximum for the CO decomposition peak centered at ≈ 610 °C is prevalently assigned to phenolic groups, its shifting around 700 °C or even higher temperature values is commonly due to carbonyl or quinone-type fragments.^{99, 101-102} The narrow peak of CO at 724 °C (Figure 3F, sample **1**) is reasonably attributed to carbonyl fragments in a moderately oxidized sample where C=O groups are at disposal at the material surface (Table 1, entry 1). For samples **3** and **4**, broader CO profiles with their maximum shifted at higher temperature values (> 700 °C) are observed instead.

To complete the materials characterization and get additional insights on their morphological properties, HRTEM images along with the respective inverse fast Fourier transform (IFFT) processing, have been recorded on samples **1-4** and are shown in Figure 4A-D and 4A'-D'. All images display similar fingerprints with an ordered domain at the inner ND cores made of crystal structures with (1 1 1) lattice fringes and a typical interspacing of 2.06 Å (marked in Figure 4).¹⁰³ The latter is in accord with the (1 1 1) diamonds facet observed

around $2\theta \approx 42^\circ$ of XRD profiles in Figure 2D. A shell of graphite is clearly observed in diamonds that underwent annealing at 1100°C (Figure 4C and 4D) whereas an increased surface disorder due to an amorphous C-phase caused by etching/restructuring/oxidation/coke deposition paths of the outer C-layers is observable in samples after ODH treatment (Figure 4A vs. 4B and 4C vs. 4D and Figure S4 a vs. b and c vs. d).

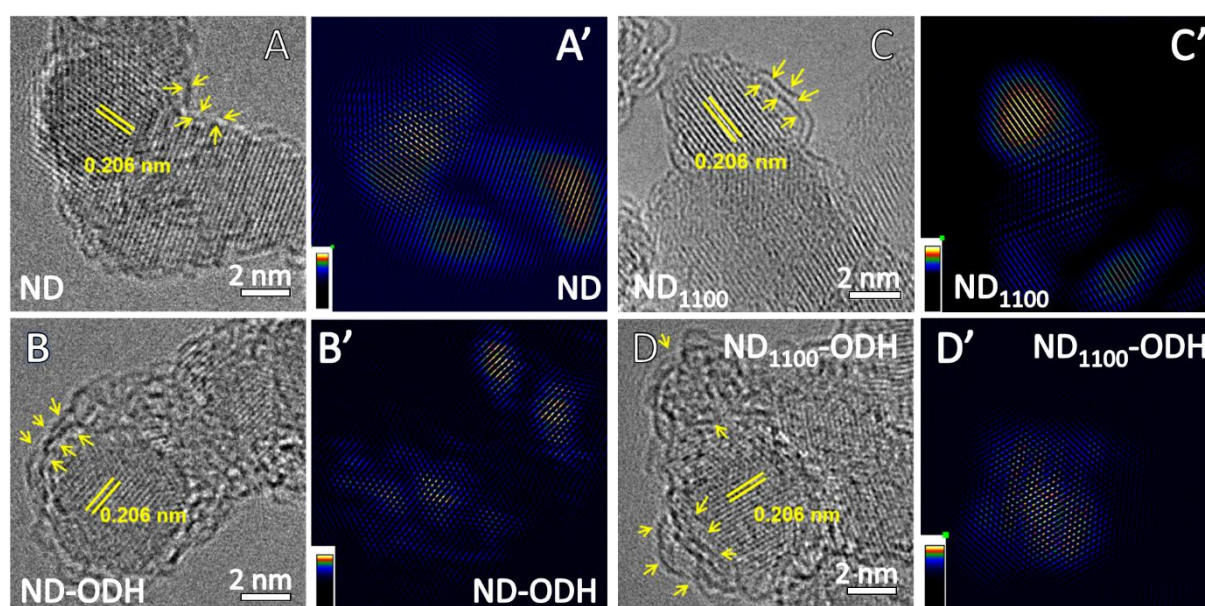


Figure 4. HR-TEM images and inverse fast Fourier transform processing of ND (1) (A and A'), ND-ODH, (3) (B and B'), ND₁₁₀₀ (2) (C and C') and ND₁₁₀₀-ODH (4) (D and D'). Intensity color (from black to yellow) in IFFT refers to the intensity of (111) pattern in the samples.

Finally, specific surface areas (SSA) and pore-size distributions of **1-4** were determined by N₂ physisorption measurements at the liquid N₂ temperature (77 K). As Figure S5 and Table S1 show, all diamonds maintained classical Type IV isothermal profiles with moderate H2 hysteresis loops in the 0.6-1.0 P/P₀ range, typical of micro- and meso-porous structures originated from the samples surface properties and aggregation phenomena among the diamond nanoparticles.⁵⁸

Despite the only moderate alterations of the morphological properties for the treated ND samples (**2-4**) respect to pristine ones (**1**), a comparative analysis led to infer that coke deposits^{62, 104-105} and the more surface disordered ODH-treated diamonds (**3** and **4**) reduced their SSA and the mesoporous sites density, whereas thermal annealing increased both (Figure S5 A,C, **1** vs. **2**).

3.3 Connection between catalytic outcomes and materials characterization: the hypothesis for oxidized sp^3 -cubic diamonds as dehydrogenation active sites under DDH conditions.

The complete set of chemico-physical, spectroscopic and morphological characterizations of diamonds before (**1**) and after exposure to thermal (**2**) and/or thermo-chemical (**3**, **4**) treatments was combined with the catalytic outcomes recorded under DDH conditions (Figure 1A' and 1B').

EPR analyses on diamond samples prompted us to rule out any hypothesis of an initiated/promoted radical reaction mechanism in the EB-to-ST conversion under DDH conditions. Indeed, the negligible intensity change in EPR signal of ND vs. ND-ODH and ND₁₁₀₀ vs. ND₁₁₀₀-ODH cannot justify the activity gap measured between these catalyst pairs (see Figure 1A' and 1B'). On a similar ground, the appreciable change in the EPR signal intensity measured between samples **1** and **2** (Figure 2A) was in contrast with the very close performance (X_{EB}) of these two catalysts at the regime conditions (blue rhombuses in Figure 1A' and 1B').

The full data set of spectroscopic data collected on samples **1-4** (EEL, Raman, XRD,

XANES and XPS spectroscopy) account for a progressive reduction of sp^3 -cubic phase of pristine nanodiamonds in favor of sp^2 -hybridized carbon networks with a variable extent of oxidized surface carbons. It is already well known that high-temperature ND annealing ($> 900\text{ }^\circ\text{C}$) initiates a surface restructuration of the sample with the generation of multi-graphite shell structures (**1** \rightarrow **2**). On the other hand, the growth of newly sp^2 -graphitized portions in the form of oxidized networks on all ODH-treated nanodiamonds (**1** \rightarrow **3** and **2** \rightarrow **4**) opens to new considerations. EELS analyses have actually demonstrated how diamonds exposure to ODH conditions favored an epitaxial growth of newly C-deposits on sp^2 -graphitized portions of diamonds. Indeed, the higher the graphitization degree of the starting C-network (**1** vs. **2**) the higher the peak intensity growth associated to sp^2 -hybridized carbons in ODH treated samples (**3** vs. **4**). The as-formed graphitized networks certainly favor (under ODH conditions) the generation of redox active C=O moieties to perform the EB-to-ST dehydrogenation. On the other hand, ODH-treated samples (**3** and **4**) were up two-fold less active than their pristine counterparts (**1** and **2**) when dehydrogenation was operated under the non-oxidative DDH conditions (Figure 1A' and 1B'; red vs. blue rhombuses). If the dramatic collapse of nanodiamonds performance (**1-4**) after removing oxygen from the reagents stream is ascribed (in part) to the endothermic nature of DDH conditions (only partially compensated by the increase of the reaction temperature from 450 to 550 $^\circ\text{C}$), a reduction of the catalytically active groups involved in the direct dehydrogenation is certainly a key contributory factor.

Given the samples surface composition, carbonyl/quinone fragments still remain the main candidates as active sites for the DDH process as well. Anyhow, the reduced performance of ODH-treated samples when re-used under oxygen-free dehydrogenation conditions (Figure

1A' and 1B'), opens to alternative oxidized carbon sources as the active sites for DDH. In particular, the increasing C_{sp^2}/C_{sp^3} ratio measured on samples **3** and **4** prompted us to evaluate carbonyl fragments generated at the edge sites of cubic- C_{sp^3} portions as the most likely groups engaged in the catalytic EB-to-ST dehydrogenation under oxygen-free conditions (DDH).

Certainly, a kinetically and thermodynamically feasible dehydrogenation mechanism will have to meet with an equally feasible regeneration path of the active groups, as to keep on the catalytic loop also when it is accomplished in a non-oxidative environment (DDH).

The following section allows to speculate on the supposed mechanistic paths for DDH by means of spin-polarized DFT calculations carried out on model substrates: 1) a cubic- sp^3 ND having an edge (non-aromatic) ortho-quinone (oQ) group, 2) a sp^2 -graphitic network bearing an edge (aromatic) oQ moiety and a sp^2/sp^3 -octahedral ND showing a mono-radical oQ fragment.

3.4 DFT calculations on a model cubic- sp^3 diamond with oxidized edge C-sites

The catalyst model was initially designed in the form of a cubic- sp^3 C-network bearing a non-aromatic, ortho-quinone group (Figure 5A, I_A). A classical C_{sp^2} -graphene framework containing a quinone group was also designed and optimized for the sake of comparison (Figure 5B, I_B). Figure 5A and 5B summarize the computed mechanistic paths whose theoretical details have been discussed afterwards. According to the literature, the first C-H bond dissociation is the rate-determining step (RDS) of the dehydrogenation process (*vide infra*) whatever the operative conditions at work (ODH or DDH).¹⁰⁶ At the same time, the oQ groups regeneration at the end of each catalytic cycle were modelled assuming a non-

oxidative environment (DDH) for the hydroxy-ketone/phenol thermal-decomposition paths (with H₂ evolution - red curves on the catalytic cycles of Figure 5).

Structures containing either oQ groups or hydroxy-ketone/phenol fragments have been optimized and used for the starting catalytic materials and their reduced forms, respectively. For the two optimized structures (I_A and I_B) involved in the EB C-H bond activation, a transition state (TS_{1,A} and TS_{1,B}) associated to the generation of the hydroxy-ketones (II_A and II_B) was found at $\Delta G^\ddagger = +28.6$ and $+24.2$ kcal·mol⁻¹, respectively (Figure 6A,C and Figure S6A). Simultaneously, gas-phase EB molecule becomes in the radical form. For both radical intermediates (II_A and II_B) two more thermodynamically favorable resonant structures (III_A and III_B) are possible through the radical migration from the C atom to the more electrophilic oxygen of the remaining ketone (see also Figure S6A).

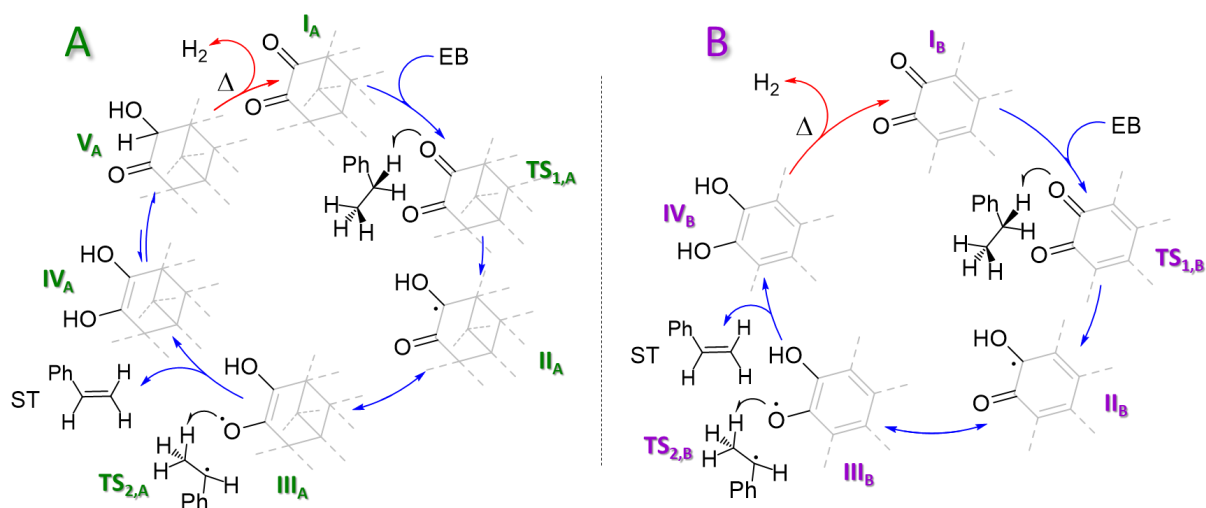


Figure 5. A) mechanistic hypothesis for a non-aromatic oQ group on cubic-sp³ NDs. B) Classical mechanistic path for an oQ group at the edge of an C_{sp2}-graphitic network. Roman numerals and TS refer to reaction intermediates and transition states. Blue arrows and red arrows refer to the EB-dehydrogenation and catalyst (oQ) regeneration paths, respectively.

As Figure 5B shows, such a resonance is even more favored in the case of C_{sp2}-graphitic networks because it is associated to the recovery of the aromatic character of the C-network.

As far as the second EB C-H bond activation is concerned, radical C-O• on intermediates (III_A and III_B) evolve into the bis-hydroxy species (IV_A and IV_B) through lower ΔG^\ddagger energy barriers of 6.2 and 13.1 kcal·mol⁻¹, respectively (see also Figure S6A).

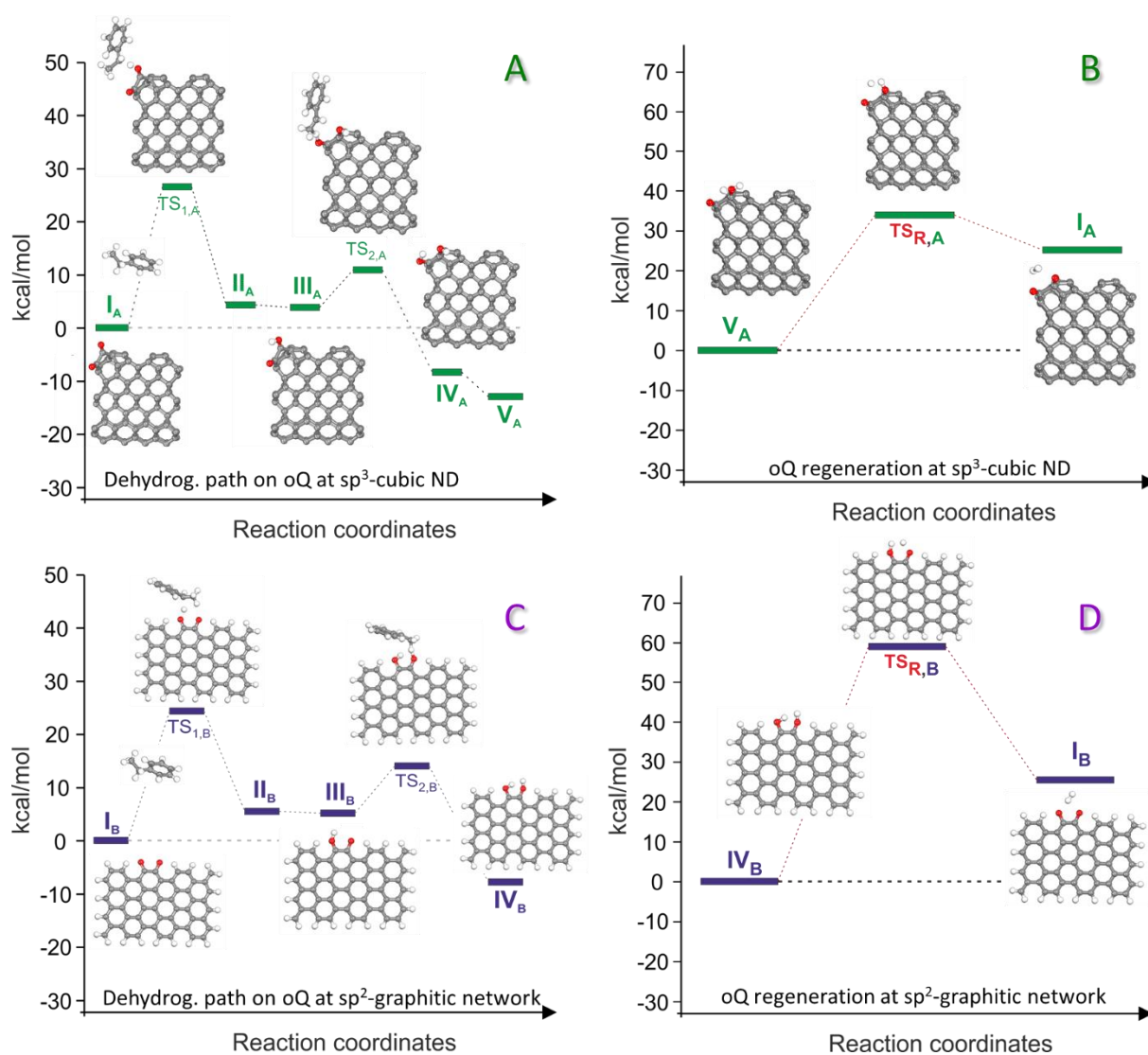


Figure 6. A) Reaction coordinates and energy profile of the EB dehydrogenation mechanism occurring on an oQ group at the edge of a sp³-cubic ND and B) the relative hydroxy-ketone regeneration path *via* thermal decomposition. C) Reaction coordinates and energy profile of the EB dehydrogenation mechanism occurring on an oQ group at a sp²-graphitic network and D) the relative bis-phenol regeneration path *via* thermal decomposition.

While IV_B is supposed to be the most thermodynamically stable bis-hydroxy intermediate at the end of the catalytic cycle, IV_A can evolve into the more stable hydroxy-ketone (V_A) *via*

keto-enolic tautomerism (Figure 5A, 6A and Figure S6A).

Both energetic profiles calculated for the two mechanistic paths are consistent with thermodynamically and kinetically feasible processes and present an energy gap associated to the first and kinetically sluggish EB C-H activation/abstraction by the oQ groups (RDS) of only $4.4 \text{ kcal}\cdot\text{mol}^{-1}$ in favor of the process promoted by an aromatic oQ group at the edge of a graphitized C_{sp^2} -network. Such a difference in the two energy profiles does not allow to claim any conclusion on the role of oQ groups at the edge of C_{sp^3} -cubic ND respect to the more abundant oQ groups located at C_{sp^2} -graphitic networks. On the contrary, a more distinctive action of oQ groups on C_{sp^3} -cubic ND can be found in their regeneration process at the end of the EB dehydrogenation step (Figure 5A, B – red arrows, Figure-6B and 6D and Figure S6B). Indeed, while thermal decomposition of the bis-phenol IV_B proceeds through a ΔG^\ddagger energy barriers of $59.7 \text{ kcal}\cdot\text{mol}^{-1}$, the hydroxy-ketone V_A presents a much lower ΔG^\ddagger energy barrier ($33.4 \text{ kcal}\cdot\text{mol}^{-1}$) to regenerate via thermal decomposition the starting oQ. The energy gap measured between the two TS ($\approx 26.3 \text{ kcal}\cdot\text{mol}^{-1}$ lower on $\text{TS}_{R,A}$; Figure S6B) can be invoked to support the hypothesis of oQ groups at the edge of C_{sp^3} -cubic diamonds as the active sites responsible for the observed catalytic performance under DDH conditions.

For the sake of completeness, we also assumed the generation of oQ groups at sp^2/sp^3 octahedral NDs (Figure S7 and S8A,B). For this optimized structure a mechanism for the EB dehydrogenation similar to that described above has pointed out the existence of largely reduced ΔG^\ddagger energy barriers ($\text{TS}_{1,C}$ and $\text{TS}_{2,C}$) respect to those calculated for the other aforementioned oQ-based catalysts (Figure S7 and S8A; see also Figure S6A). A relatively higher energy barrier ($47.3 \text{ kcal}\cdot\text{mol}^{-1}$), associated to the decomposition of intermediate III_C

(for the regeneration of I_C) was finally calculated for this hybrid structure (Figure S6B). Anyhow, a direct involvement of this radical hybrid structure in the direct dehydrogenation process is unlikely to occur for the reasons outlined above.

4. Conclusions

To summarize, the full set of spectroscopic, spectrometric and microscopic data collected on samples **1-4** gives an account of the followings:

- 1) ODH conditions result in a progressive reduction of the sp^3 -cubic phase of nanodiamonds in favor of a sp^2 -hybridized carbon phase with a variable extent of oxidized surface carbons. Given the moderate temperature conditions of ODH catalysis, it seems reasonable to consider such an effect as the formation of new C-deposits (coking) epitaxially grown on sp^2 -graphitized portions of diamonds rather than a temperature-induced diamonds surface restructuring. Moreover, the higher the graphitization degree of the starting C-network (*i.e.* **1** \rightarrow **3** and **2** \rightarrow **4**), the higher the percentage of variably oxidized C_{sp^2} deposits formed during ODH.
- 2) Nanodiamonds increasing their C_{sp^2}/C_{sp^3} ratio (**3** and **4**) show increased catalytic performance under oxidative atmosphere (ODH) whereas their ability to convert EB to ST under oxygen-free conditions (DDH) is reduced by half compared to that of pristine samples (**1** and **2** - not submitted to ODH treatment).
- 3) Samples characterization has established that ketones are ubiquitous and they remain the main form of oxidized carbon to be claimed as active sites for the DDH process as well. However, catalytic outcomes have suggested that ketones/quinones functionalities from

C_{sp^2} networks are poorly active if not inactive for dehydrogenation under oxygen-free conditions (DDH). The absence of an oxidizing environment implies that a kinetically and thermodynamically feasible regeneration path of the reduced ketones (alternative to that occurring under ODH conditions), will take place as to close the catalytic loop. This has prompted us to consider a cubic- sp^3 ND having an edge (non-aromatic) ortho-quinone (oQ) group as an alternative oxidized carbon source for the DDH active sites.

Our hypothesis for an oQ group at the edge of a cubic- sp^3 ND has been modeled in silico and compared with the energy profile of a classical oQ group at the edge of a sp^2 -graphitic network at the applied reaction conditions. The comparative analysis of the two energy profiles in the EB dehydrogenation did not allow to infer any conclusion on the role of oQ groups at the edge of C_{sp^3} -cubic ND respect to the oQ groups on C_{sp^2} -graphitic networks. On the other hand, the regeneration paths of the oQ reduced forms via thermal decomposition has unveiled a much lower energy barrier [$\approx -26.3 \text{ kcal}\cdot\text{mol}^{-1}$ as $\Delta(ST_{R,A}-ST_{R,B})$] associated to the regeneration of the former oQ unit.

Such an energy gap between the two TS supports the hypothesis of oQ groups at the edge of C_{sp^3} -cubic diamonds as the active sites engaged for the catalytic EB dehydrogenation when the reaction is operated under oxygen-free conditions.

ASSOCIATED CONTENT

Supporting Information. This material is available free of charge via the Internet at <http://pubs.acs.org>.”

AUTHOR INFORMATION

Corresponding Authors

Yuefeng Liu - Dalian National Laboratory for Clean Energy, Dalian Institute of Chemical Physics, Chinese Academy of Sciences; Dalian 116023, China.; Email: yuefeng.liu@dicp.ac.cn

Giuliano Giambastiani - Institute of Chemistry and Processes for Energy, Environment and Health (ICPEES), UMR 7515 CNRS-University of Strasbourg, 25 rue Becquerel, 67087 Strasbourg Cedex 02, France and Institute of Chemistry of Organometallic Compounds, ICCOM-CNR and Consorzio INSTM, Via Madonna del Piano, 10-50019, Sesto F.no, Florence, Italy. Email: giambastiani@unistra.fr and giuliano.giambastiani@iccom.cnr.it

Author Contributions

‡ L.F. and S.A. contributed equally.

Notes

The authors declare no competing financial interest.

ACKNOWLEDGMENT

This work was financially supported by the NSFC of China (Nos. 21972140 and 21872144), CAS Youth Innovation Promotion Association (2018220), LiaoNing Revitalization Talents Program (XLYC1907053). G. G. and C. P.-H. thank the TRAINER project (Catalysts for Transition to Renewable Energy Future) of the “Make our Planet Great

Again” program (Ref. ANR-17-MPGA-0017) for support. G. G. and G. T. would also like to thank the Italian MIUR through the PRIN 2017 Project Multi-e (20179337R7) “Multielectron transfer for the conversion of small molecules: an enabling technology for the chemical use of renewable energy” for financial support to this work. Y. L. and G. G. finally thank the CAS President’s International Fellowship Initiative (PIFI) program for support. XAS experiments were conducted at the MCD Endstation at the BL12B-a beamline in the National Synchrotron Radiation Laboratory (NSRL) in Hefei, China. Prof. Wensheng Yan (NSRL) is kindly acknowledged for his assistance on XAS analysis. The authors acknowledged Profs. Qiang Fu (DICP) and Jingjie Luo (DUT) for their fruitful discussion and assistance during the manuscript preparation.

REFERENCES AND NOTES

1. Yun, Y. S.; Lee, M.; Sung, J.; Yun, D.; Kim, T. Y.; Park, H.; Lee, K. R.; Song, C. K.; Kim, Y.; Lee, J., *et al.*, Promoting effect of cerium on MoVTaNb mixed oxide catalyst for oxidative dehydrogenation of ethane to ethylene. *Appl. Catal. B, Environ.* **2018**, *237*, 554–562.
2. Luo, L.; You, R.; Liu, Y.; Yang, J.; Zhu, Y.; Wen, W.; Pan, Y.; Qi, F.; Huang, W., Gas-Phase Reaction Network of Li/MgO-Catalyzed Oxidative Coupling of Methane and Oxidative Dehydrogenation of Ethane. *ACS Catal.* **2019**, *9*, 2514-2520.
3. Bautista, F. M.; Campelo, J. M.; Luna, D.; Marinas, J. M.; Quirós, R. A.; Romero, A. A., Screening of amorphous metal–phosphate catalysts for the oxidative dehydrogenation of ethylbenzene to styrene. *Appl. Catal. B, Environ.* **2007**, *70*, 611-620.

4. Tajeddin, B.; Ahmadi, B.; Sohrab, F.; Chenarbon, H. A., Polymers for Modified Atmosphere Packaging Applications. In *Food Packaging and Preservation*, Grumezescu, A. M.; Holban, A. M., Eds. Academic Press: 2018; pp 457-499.
5. CHEMANALYST, Styrene Market Analysis: Plant Capacity, Production, Operating Efficiency, Technology, Demand & Supply, Application, Distribution Channel, Regional Demand, 2015-2030 <https://www.chemanalyst.com/industry-report/styrene-market-650>. Last access on January, 2022.
6. Meyers, R. A., Polimeri Europa Styrene Process Technology. In *Handbook of petrochemicals production processes*, McGraw-Hill Education: New York, 2005.
7. Su, D. S.; Perathoner, S.; Centi, G., Nanocarbons for the development of advanced catalysts. *Chem. Rev.* **2013**, *113* (8), 5782-5816.
8. Zhao, Z.; Ge, G.; Li, W.; Guo, X.; Wang, G., Modulating the microstructure and surface chemistry of carbocatalysts for oxidative and direct dehydrogenation: A review. *Chin. J. Catal.* **2016**, *37*, 644-670.
9. Su, D. S.; Zhang, J.; Frank, B.; Thomas, A.; Wang, X.; Paraknowitsch, J.; Schlögl, R., Metal - Free Heterogeneous Catalysis for Sustainable Chemistry. *ChemSusChem* **2010**, *22*, 169-180.
10. Qi, W.; Su, D., Metal-Free Carbon Catalysts for Oxidative Dehydrogenation Reactions. *ACS Catal.* **2014**, *4* (9), 3212-3218.
11. Chizari, K.; Deneuve, A.; Ersen, O.; Florea, I.; Liu, Y.; Edouard, D.; Janowska, I.; Begin, D.; Pham - Huu, C., Nitrogen - doped carbon nanotubes as a highly active metal - free catalyst for selective oxidation. *ChemSusChem* **2012**, *5* (1), 102-108.

12. Xu, C.; Chen, J.; Li, S.; Gu, Q.; Wang, D.; Jiang, C.; Liu, Y., N-doped honeycomb-like porous carbon derived from biomass as an efficient carbocatalyst for H₂S selective oxidation. *J. Hazard. Mater.* **2021**, *403*, 123806.
13. Xu, C.; Gu, Q.; Li, S.; Ma, J.; Zhou, Y.; Zhang, X.; Jiang, C.; Pham-Huu, C.; Liu, Y., Heteroatom-Doped Monolithic Carbocatalysts with Improved Sulfur Selectivity and Impurity Tolerance for H₂S Selective Oxidation. *ACS Catal.* **2021**, *11*, 8591-8604.
14. Ba, H.; Luo, J.; Liu, Y.; Duong-Viet, C.; Tuci, G.; Giambastiani, G.; Nhut, J.-M.; Nguyen Dinh, L.; Ersen, O.; Su, D. S., *et al.*, Macroscopically shaped monolith of nanodiamonds @nitrogen-enriched mesoporous carbon decorated SiC as a superior metal-free catalyst for the styrene production. *Appl. Catal. B, Environ.* **2017**, *200*, 343-350.
15. Diao, J.; Feng, Z.; Huang, R.; Liu, H.; Hamid, S. B. A.; Su, D. S., Selective and Stable Ethylbenzene Dehydrogenation to Styrene over Nanodiamonds under Oxygen-lean Conditions. *ChemSusChem* **2016**, *9*, 662-669.
16. Ba, H.; Liu, Y.; Truong-Phuoc, L.; Duong-Viet, C.; Nhut, J.-M.; Nguyen, D. L.; Ersen, O.; Tuci, G.; Giambastiani, G.; Pham-Huu, C., N-doped food-grade-derived 3D mesoporous foams as metal-free systems for catalysis. *ACS Catal.* **2016**, *6* (3), 1408-1419.
17. Li, M.; Xu, F.; Li, H.; Wang, Y., Nitrogen-doped porous carbon materials: promising catalysts or catalyst supports for heterogeneous hydrogenation and oxidation. *Catal. Sci. Technol.* **2016**, *6*, 3670-3693.
18. Luo, J.; Peng, F.; Wang, H.; Yu, H., Enhancing the catalytic activity of carbon nanotubes

- by nitrogen doping in the selective liquid phase oxidation of benzyl alcohol. *Catal. Commun.* **2013**, *39*, 44-49.
19. Tuci, G.; Pilaski, M.; Ba, H.; Rossin, A.; Luconi, L.; Caporali, S.; Pham-Huu, C.; Palkovits, R.; Giambastiani, G., Unraveling Surface Basicity and Bulk Morphology Relationship on Covalent Triazine Frameworks with Unique Catalytic and Gas Adsorption Properties. *Adv. Funct. Mater.* **2017**, *27*, 1605672.
 20. Tuci, G.; Iemhoff, A.; Ba, H.; Luconi, L.; Rossin, A.; Papaefthimiou, V.; Palkovits, R.; Artz, J.; Pham-Huu, C.; Giambastiani, G., Playing with Covalent Triazine Framework Tiles for Improved CO₂ Adsorption Properties and Catalytic Performance. *Beilstein J. Nanotechnol.* **2019**, *10*, 1217-1227.
 21. Ba, H.; Tuci, G.; Evangelisti, C.; Ceppatelli, M.; Lam, N.-D.; Dal Santo, V.; Bossola, F.; Nhut, J.-M.; Rossin, A.; Granger, P., *et al.*, Second Youth of a Metal-Free Dehydrogenation Catalyst: When γ -Al₂O₃ Meets Coke Under Oxygen- and Steam-Free Conditions. *ACS Catal.* **2019**, *9* (10), 9474-9484.
 22. Duong-Viet, C.; Nhut, J.-M.; Truong-Huu, T.; Tuci, G.; Nguyen-Dinh, L.; Pham, C.; Giambastiani, G.; Pham-Huu, C., Tailoring Properties of Metal-Free Catalysts for the Highly Efficient Desulfurization of Sour Gases under Harsh Conditions. *Catalysts* **2021**, *11*, 226.
 23. Tang, C.; Zhang, Q., Nanocarbon for oxygen reduction electrocatalysis: dopants, edges, and defects. *Adv. Mater.* **2017**, *29* (13), 1604103.
 24. Gong, K.; Du, F.; Xia, Z.; Durstock, M.; Dai, L., Nitrogen-doped carbon nanotube arrays with high electrocatalytic activity for oxygen reduction. *Science* **2009**, *323*

- (5915), 760-764.
25. Yang, L.; Shui, J.; Du, L.; Shao, Y.; Liu, J.; Dai, L.; Hu, Z., Carbon - based metal - free ORR electrocatalysts for fuel cells: past, present, and future. *Adv. Mater.* **2019**, *31* (13), 1804799.
 26. Zhang, L.; Jia, Y.; Yan, X.; Yao, X., Activity Origins in Nanocarbons for the Electrocatalytic Hydrogen Evolution Reaction. *Small* **2018**, 1800235.
 27. Zhao, S.; Wang, D.-W.; Amal, R.; Dai, L., Carbon-Based Metal-Free Catalysts for Key Reactions Involved in Energy Conversion and Storage. *Adv. Mater.* **2018**, *31*, 1801526.
 28. Tuci, G.; Filippi, J.; Ba, H.; Rossin, A.; Luconi, L.; Pham-Huu, C.; Vizza, F.; Giambastiani, G., How to Teach an Old Dog New (Electrochemical) Tricks: Aziridine-Functionalized CNTs as Efficient Electrocatalysts for the Selective CO₂ Reduction to CO. *J. Mater. Chem. A* **2018**, *6*, 16382-16389.
 29. Tuci, G.; Filippi, J.; Rossin, A.; Luconi, L.; Pham-Huu, C.; Yakhvarov, D.; Vizza, F.; Giambastiani, G., CO₂ Electrochemical Reduction by Exohedral N-Pyridine Decorated Metal-Free Carbon Nanotubes. *Energies* **2020**, *13*, 2703.
 30. Duong-Viet, C.; Nhut, J.-M.; Truong-Huu, T.; Tuci, G.; Nguyen-Dinh, L.; Liu, Y.; Pham, C.; Giambastiani, G.; Pham-Huu, C., A nitrogen-doped carbon-coated silicon carbide as a robust and highly efficient metal-free catalyst for sour gas desulfurization in the presence of aromatics as contaminants. *Catal. Sci. Technol.* **2020**, *10*, 5487-5500.
 31. Zhu, Y.; Lin, Y.; Zhang, B.; Rong, J.; Zong, B.; Su, D. S., Nitrogen-Doped Annealed Nanodiamonds with Varied sp²/sp³ Ratio as Metal-Free Electrocatalyst for the Oxygen Reduction Reaction. *ChemCatChem* **2015**, *7*, 2840-2845.

32. Duan, X.; Ao, Z.; Sun, H.; Indrawirawan, S.; Wang, Y.; Kang, J.; Liang, F.; Zhu, Z. H.; Wang, S., Nitrogen-Doped Graphene for Generation and Evolution of Reactive Radicals by Metal-Free Catalysis. *ACS Appl. Mater. Interfaces* **2015**, *7*, 4169-4178.
33. Yang, Y.; Zhang, W.; Ma, X.; Zhao, H.; Zhang, X., Facile Construction of Mesoporous NDoped Carbons as Highly Efficient 4-Nitrophenol Reduction Catalysts. *ChemCatChem* **2015**, *7*, 3454-3459.
34. Tuci, G.; Rossin, A.; Luconi, L.; Pham-Huu, C.; Cicchi, S.; Ba, H.; Giambastiani, G., Pyridine-Decorated Carbon Nanotubes as a Metal-Free Heterogeneous Catalyst for Mild CO₂ Reduction to Methanol with Hydroboranes. *Catal. Sci. Technol.* **2017**, *7*, 5833-5837.
35. Chen, S. S.; Carraher, J. M.; Tuci, G.; Rossin, A.; Raman, C. A.; Luconi, L.; Tsang, D. C. W.; Giambastiani, G.; Tessonnier, J.-P., Tailoring the Amine Microenvironment in N-Decorated C-Networks: How to Improve Carbocatalysts' Performance for the Glucose-to-Fructose Isomerization. *ACS Sustain. Chem. Eng.* **2019**, *7*, 16959-16963.
36. Zhang, J.; Su, D. S.; Blume, R.; Schlögl, R.; Wang, R.; Yang, X.; Gajović, A., Surface chemistry and catalytic reactivity of a nanodiamond in the steam - free dehydrogenation of ethylbenzene. *Angew. Chem. Int. Ed.* **2010**, *49*, 8640-8644.
37. Zhao, Z.; Dai, Y.; Lin, J.; Wang, G., Highly-Ordered Mesoporous Carbon Nitride with Ultrahigh Surface Area and Pore Volume as a Superior Dehydrogenation Catalyst. *Chem. Mater.* **2014**, *26*, 3151-3161.
38. Guifang, G.; Zhao, Z., Nanodiamond@carbon nitride hybrid with loose porous carbon nitride layers as an efficient metal-free catalyst for direct dehydrogenation of

- ethylbenzene. *Appl. Catal. A* **2018**, *571*, 82-88.
39. Zhou, Q.; Zhao, Z., Sulfate Surfactant Assisted Approach to Fabricate Sulphur-Doped Supported Nanodiamond Catalyst on Carbon Nanotube with Unprecedented Catalysis for Ethylbenzene Dehydrogenation. *ChemCatChem* **2020**, *12*, 342-349.
40. Tian, S.; Yan, P.; Li, F.; Zhang, X.; Su, D.; Qi, W., Fabrication of Polydopamine Modified Carbon Nanotube Hybrids and their Catalytic Activity in Ethylbenzene Dehydrogenation. *ChemCatChem* **2019**, *11*, 2073-2078.
41. Nederlof, C.; Zarubina, V.; Melián-Cabrera, I. V.; Heeres, E. H. J.; Kapteijn, F.; Makkee, M., Application of staged O₂ feeding in the oxidative dehydrogenation of ethylbenzene to styrene over Al₂O₃ and P₂O₅/SiO₂ catalysts. *Appl. Catal. A* **2014**, *476*, 204-214.
42. Zhang, J.; Liu, X.; Blume, R.; Zhang, A.; Schlögl, R.; Su, D. S., Surface-modified carbon nanotubes catalyze oxidative dehydrogenation of n-butane. *Science* **2008**, *322* (5898), 73-77.
43. Qi, W.; Liu, W.; Zhang, B.; Gu, X.; Guo, X.; Su, D., Oxidative Dehydrogenation on Nanocarbon: Identification and Quantification of Active Sites by Chemical Titration. *Angew. Chem. Int. Ed.* **2013**, *52* (52), 14224-14228.
44. Qi, W.; Liu, W.; Guo, X.; Schlögl, R.; Su, D., Oxidative dehydrogenation on nanocarbon: Intrinsic catalytic activity and structure–function relationships. *Angew. Chem. Int. Ed.* **2015**, *54* (46), 13682-13685.
45. Liu, X.; Frank, B.; Zhang, W.; Cotter, T. P.; Schlögl, R.; Su, D. S., Carbon - catalyzed oxidative dehydrogenation of n - butane: selective site formation during sp³ - to - sp² lattice rearrangement. *Angew. Chem. Int. Ed.* **2011**, *50* (14), 3318-3322.

46. Liang, C.; Xie, H.; Schwartz, V.; Howe, J.; Dai, S.; Overbury, S. H., Open-Cage Fullerene-like Graphitic Carbons as Catalysts for Oxidative Dehydrogenation of Isobutane. *J. Am. Chem. Soc.* **2009**, *131*, 7735-7741.
47. Macià-Agullò, J. A.; Cazorla-Amoròs, D.; Linares-Solano, A.; Wild, U.; Su, D. S.; Schlögl, R., Oxygen functional groups involved in the styrene production reaction detected by quasi in situ XPS. *Catal. Today* **2005**, *102*, 248-253.
48. Liu, W.; Wang, C.; Su, D. S.; Qi, W., Oxidative dehydrogenation of ethylbenzene on nanocarbon: Kinetics and reaction mechanism. *J. Catal.* **2018**, *368*, 1-7.
49. Węgrzyniak, A.; Jarczewski, S.; Kuśtrowski, P.; Michoreczyk, P., Influence of carbon precursor on porosity, surface composition and catalytic behaviour of CMK-3 in oxidative dehydrogenation of propane to propene. *J. Porous. Mater.* **2018**, *25*, 687-696.
50. Dathar, G. K. P.; Tsai, Y.-T.; Gierszal, K.; Xu, Y.; Liang, C.; Rondinone, A. J.; Overbury, S. H.; Schwartz, V., Identifying Active Functionalities on Few-Layered Graphene Catalysts for Oxidative Dehydrogenation of Isobutane. *ChemSusChem* **2014**, *7*, 483-491.
51. Cao, L.; Dai, P.; Zhu, L.; Yan, L.; Chen, R.; Liu, D.; Gu, X.; Li, L.; Xue, Q.; Zhao, X., Graphitic carbon nitride catalyzes selective oxidative dehydrogenation of propane. *Appl. Catal. B, Environ.* **2020**, *262*, 118277.
52. Qi, W.; Yan, P.; Su, D. S., Oxidative Dehydrogenation on Nanocarbon: Insights into the Reaction Mechanism and Kinetics via in Situ Experimental Methods. *Acc. Chem. Res.* **2018**, *51*, 640-648.
53. Liu, L.; Deng, Q.-F.; Agula, B.; Ren, T.-Z.; Liu, Y.-P.; Zhaorigetu, B.; Yuan, Z.-Y.,

- Synthesis of ordered mesoporous carbon materials and their catalytic performance in dehydrogenation of propane to propylene. *Catal. Today* **2012**, *186*, 35-41.
54. Liu, L.; Deng, Q.-F.; Agula, B.; Zhao, X.; Ren, T.-Z.; Yuan, Z.-Y., Ordered mesoporous carbon catalyst for dehydrogenation of propane to propylene. *Chem. Commun.* **2011**, *47*, 8334-8336.
 55. Liu, L.; Deng, Q.-F.; Liu, Y.-P.; Ren, T.-Z.; Yuan, Z.-Y., HNO₃-activated mesoporous carbon catalyst for direct dehydrogenation of propane to propylene. *Catal. Commun.* **2011**, *16*, 81-85.
 56. Liu, T.-F.; Ali, S.; Li, B.; Su, D. S., Revealing the Role of sp²@sp³ Structure of Nanodiamond in Direct Dehydrogenation: Insight from DFT study. *ACS Catal.* **2017**, *7*, 3779–3785.
 57. Zhao, Z.; Li, W.; Dai, Y.; Ge, G.; Guo, X.; Wang, G., Carbon Nitride Encapsulated Nanodiamond Hybrid with Improved Catalytic Performance for Clean and Energy-Saving Styrene Production via Direct Dehydrogenation of Ethylbenzene. *ACS Sustainable Chem. Eng.* **2015**, *3*, 3355-3364.
 58. Duan, X.; Ao, Z.; Zhang, H.; Saunders, M.; Sun, H.; Shao, Z.; Wang, S., Nanodiamonds in sp²/sp³ configuration for radical to nonradical oxidation: Core-shell layer dependence. *Appl. Catal. B, Environ.* **2018**, *222*, 176-181.
 59. Zhang, J.; Su, D. S.; Zhang, A.; Wang, D.; Schlögl, R.; Hébert, C., Nanocarbon as Robust Catalyst: Mechanistic Insight into Carbon-Mediated Catalysis. *Angew. Chem. Int. Ed.* **2007**, *46*, 7319-7323.
 60. Su, D. S.; Maksimova, N. I.; Mestl, G.; Kuznetsov, V. L.; Keller, V.; Schlögl, R.; Keller,

- N., Oxidative dehydrogenation of ethylbenzene to styrene over ultra-dispersed diamond and onion-like carbon. *Carbon* **2007**, *45*, 2145-2151.
61. Kurakami, Y.; Iwayama, K.; Uchida, H.; Hattori, T.; Tagawa, T., Screening of catalysts for the oxidative dehydrogenation of ethylbenzene. *Appl. Catal.* **1982**, *2*, 67-74.
62. Zarubina, V.; Talebi, H.; Jansma, H.; Góra-Marek, K.; Nederlof, C.; Kapteijn, F.; Makkee, M.; Melián-Cabrera, I., On the thermal stabilization of carbon-supported SiO₂ catalysts by phosphorus: Evaluation in the oxidative dehydrogenation of ethylbenzene to styrene and a comparison with relevant catalysts. *Appl. Catal. A* **2016**, *514*, 173-181.
63. Ba, H.; Liu, Y.; Mu, X.; Doh, W.-H.; Nhut, J.-M.; Granger, P.; Pham-Huu, C., Macroscopic nanodiamonds/ β -SiC composite as metal-free catalysts for steam-free dehydrogenation of ethylbenzene to styrene. *Appl. Catal. A, Gen.* **2015**, *499*, 217-226.
64. Schrand, A. M.; Ciftan Hens, S. A.; Shenderova, O. A., Nanodiamond Particles: Properties and Perspectives for Bioapplications. *Crit. Rev. Solid State Mater. Sci.* **2009**, *34*, 18-74.
65. Perdew, J. P.; Ruzsinszky, A.; Csonka, G. I.; Vydrov, O. A.; Scuseria, G. E.; Constantin, L. A.; Zhou, X.; Burke, K., Restoring the Density-Gradient Expansion for Exchange in Solids and Surfaces. *Phys. Rev. Lett.* **2008**, *100*, 136406.
66. Kresse, G.; Furthmüller, J., Efficiency of ab-initio total energy calculations for metals and semiconductors using a plane-wave basis set. *Comput. Mater. Sci.* **1996**, *6*, 15-50.
67. Kresse, G.; Furthmüller, J., Efficient iterative schemes for total-energy calculations using a plane-wave basis set. *Phys. Rev. B* **1996**, *54*, 11169-11186.
68. Kresse, G.; Hafner, J., Ab initio molecular dynamics for liquid metals. *Phys. Rev. B*

- 1993**, 47, 558-561.
69. Grimme, S.; Antony, J.; Ehrlich, S.; Krieg, H., A consistent and accurate ab initio parametrization of density functional dispersion correction (DFT-D) for the 94 elements H-Pu. *J. Chem. Phys.* **2010**, 132, 154104.
 70. Henkelman, G.; Uberuaga, B. P.; Jónsson, H., A climbing image nudged elastic band method for finding saddle points and minimum energy paths. *J. Chem. Phys.* **2000**, 113, 9901-9904.
 71. Soltamova, A. A.; Ilyin, I. V.; Baranov, P. G.; Vul', A. Y.; Kidalov, S. V.; Shakhov, F. M.; Mamin, G. V.; Orlinskii, S. B.; Silkin, N. I.; Salakhov, M. K., Detection and identification of nitrogen defects in nanodiamond as studied by EPR. *Phys. B: Condens. Matter.* **2009**, 404, 4518-4521.
 72. Hoinkis, M.; Tober, E. D.; White, R. L.; Crowder, M. S., Paramagnetic centers of amorphous carbon thin films: Influence of hydrogen content and O₂ permeation. *Appl. Phys. Lett.* **1992**, 61 (22), 2653-2655.
 73. Conway, N. M. J.; Ilie, A.; Robertson, J.; Milne, W. I.; Tagliaferro, A., Reduction in defect density by annealing in hydrogenated tetrahedral amorphous carbon. *Appl. Phys. Lett.* **1998**, 73, 2456-2458.
 74. All EEL profiles are normalized to the main peak located at 290.0 eV.
 75. Muller, J. O.; Su, D. S.; Wild, U.; Schlogl, R., Bulk and surface structural investigations of diesel engine soot and carbon black. *Phys. Chem. Chem. Phys.* **2007**, 9, 4018-4025.
 76. Wang, R.; Sun, X.; Zhang, B.; Sun, X.; Su, D., Hybrid Nanocarbon as a Catalyst for Direct Dehydrogenation of Propane: Formation of an Active and Selective Core-Shell

- sp²/sp³Nanocomposite Structure. *Chem. Eur. J.* **2014**, *20* (21), 6324-6331.
77. Mochalin, V.; Osswald, S.; Gogotsi, Y., Contribution of functional groups to the Raman spectrum of nanodiamond powders. *Chem. Mater.* **2009**, *21*, 273-279.
78. Mykhaylyk, O. O.; Solonin, Y. M.; Batchelder, D. N.; Brydson, R., Transformation of nanodiamond into carbon onions: A comparative study by high-resolution transmission electron microscopy, electron energy-loss spectroscopy, x-ray diffraction, small-angle x-ray scattering, and ultraviolet Raman spectroscopy. *J. Appl. Phys.* **2005**, *97*, 074302.
79. Chen, J.; Deng, S. Z.; Chen, J.; Yu, Z. X.; Xu, N. S., Graphitization of nanodiamond powder annealed in argon ambient. *Appl. Phys. Lett.* **1999**, *74*, 3651-3653.
80. Rodil, S. E.; Ferrari, A. C.; Robertson, J.; Milne, W. I., Raman and infrared modes of hydrogenated amorphous carbon nitride. *J. Appl. Phys.* **2001**, *89*, 5425 (6).
81. Williams, O. A.; Hees, J.; Dieker, C.; Jäger, W.; Kirste, L.; Nebel, C. E., Size-Dependent Reactivity of Diamond Nanoparticles. *ACS Nano* **2010**, *4*, 4824-4830.
82. Lin, Y.; Sun, X.; Su, D. S.; Centi, G.; Perathoner, S., Catalysis by hybrid sp² /sp³ nanodiamonds and their role in the design of advanced nanocarbon materials. *Chem. Soc. Rev.* **2018**, *47*, 8438-8473.
83. Zou, Q.; Wang, M. Z.; Li, Y. G., Analysis of the nanodiamond particle fabricated by detonation. *J. Exp. Nanosci.* **2010**, *5*, 319-328.
84. Manoj, B.; Kunjomana, A. G., Study of Stacking Structure of Amorphous Carbon by X-Ray Diffraction Technique. *Int. J. Electrochem. Sci.* **2012**, *7*, 3127-3134.
85. Hemraj-Benny, T.; Banerjee, S.; Sambasivan, S.; Balasubramanian, M.; Fischer, D. A.; Eres, G.; Poretzky, A. A.; Geohegan, D. B.; Lowndes, D. H.; Han, W., *et al.*, Near-Edge

X-ray Absorption Fine Structure Spectroscopy as a Tool for Investigating Nanomaterials.

Small **2006**, *2*, 26-35.

86. Lee, V.; Dennis, R. V.; Schultz, B. J.; Jaye, C.; Fischer, D. A.; Banerjee, S., Soft X-ray Absorption Spectroscopy Studies of the Electronic Structure Recovery of Graphene Oxide upon Chemical Defunctionalization. *J. Phys. Chem. C* **2012**, *116*, 20591-20599.
87. Chuang, C.-H.; Wang, Y.-F.; Shao, Y.-C.; Yeh, Y.-C.; Wang, D.-Y.; Chen, C.-W.; Chiou, J.-W.; Ray, S. C.; Pong, W. F.; Zhang, L., *et al.*, The Effect of Thermal Reduction on the Photoluminescence and Electronic Structures of Graphene Oxides. *Sci. Rep.* **2014**, *4*, 4525 (7 pp).
88. Hua, W.; Gao, B.; Li, S.; Agren, H.; Luo, Y., X-ray absorption spectra of graphene from first-principles simulations. *Phys. Rev. B* **2010**, *82*, 155433-155439.
89. Buijsters, J. G.; Gago, R.; Redondo-Cubero, A.; Jimenez, I., Hydrogen stability in hydrogenated amorphous carbon films with polymerlike and diamond-like structure. *J. Appl. Phys.* **2012**, *112*, 093502 (7 pp).
90. Myers, C. E.; Bergmann, K. D.; Sun, C.-Y.; Boekelheide, N.; Knoll, A. H.; Gilbert, P. U. P. A., Exceptional preservation of organic matrix and shell microstructure in a Late Cretaceous Pinna fossil revealed by photoemission electron spectromicroscopy. *Earth Planet Sci. Lett.* **2018**, *46*, 711-714.
91. Chuang, C.-H.; Ray, S. C.; Mazumder, D.; Sharma, S.; Ganguly, A.; Papakonstantinou, P.; Chiou, J.-W.; Tsai, H.-M.; Shiu, H.-W.; Chen, C.-H., *et al.*, Chemical Modification of Graphene Oxide by Nitrogenation: An X-ray Absorption and Emission Spectroscopy Study. *Sci. Rep.* **2017**, *7*, 42235 (10 pp).

92. Kim, K.; Zhu, P.; Li, N.; Ma, X.; Chen, Y., Characterization of oxygen containing functional groups on carbon materials with oxygen K-edge X-ray absorption near edge structure spectroscopy. *Carbon* **2011**, *49*, 1745-1751.
93. Shestakov, M. S.; Vul', S. P.; Dideikin, A. T.; Larionova, T. V.; Shvidchenko, A. V.; Yudina, E. B.; Shnitov, V. V., Advanced oxidation process for detonation nanodiamond surface chemical modification. *J. Phys.: Conf. Ser* **2019**, *1400*, 055044.
94. Petit, T.; Arnault, J.-C.; Girard, H. A.; Sennour, M.; Bergonzo, P., Early stages of surface graphitization on nanodiamond probed by x-ray photoelectron spectroscopy. *Phys. Rev. B* **2011**, *84*, 233407.
95. Arnault, J.-C.; Petit, T.; Girard, H.; Chavanne, A.; Gesset, C.; Sennour, M.; Chaigneau, M., Surface chemical modifications and surface reactivity of nanodiamonds hydrogenated by CVD plasma. *Phys. Chem. Chem. Phys.* **2011**, *13*, 11481-11487.
96. Arnault, J.-C., X-ray Photoemission Spectroscopy applied to nanodiamonds: From surface chemistry to in situ reactivity. *Diam. Relat. Mater.* **2018**, *84*, 157-168.
97. Garen Kwan, Y. C.; Meng Ng, G.; Alfred Huan, C. H., Identification of functional groups and determination of carboxyl formation temperature in graphene oxide using the XPS O 1s spectrum. *Thin Solid Films* **2015**, *590*, 40-48.
98. Sotoma, S.; Akagi, K.; Hosokawa, S.; Igarashi, R.; Tochio, H.; Haradae, Y.; Shirakawa, M., Comprehensive and quantitative analysis for controlling the physical/chemical states and particle properties of nanodiamonds for biological applications. *RSC Adv.* **2015**, *5*, 13818-13827.
99. Tribolet, P.; Kiwi-Minsker, L., Palladium on carbon nanofibers grown on metallic filters

- as novel structured catalyst. *Catal. Today* **2005**, *105*, 337-343.
100. Rosenthal, D.; Ruta, M.; Schlögl, R.; Kiwi-Minsker, L., Combined XPS and TPD study of oxygen-functionalized carbon nanofibers grown on sintered metal fibers. *Carbon* **2010**, *48* (6), 1835-1843.
101. Figueiredo, J. L.; Pereira, M. F. R.; Freitas, M. M. A.; Orfao, J. J. M., Modification of the surface chemistry of activated carbons. *Carbon* **1999**, *37*, 1379-1389.
102. Zielke, U.; Huttinger, K. J.; Hoffman, W. P., Surface-Oxidized Carbon Fibers: I. Surface Structure and Chemistry. *Carbon* **1996**, *34*, 983-998.
103. Nemeth, P.; Garvie, L. A. J.; Buseck, P. R., Twinning of cubic diamond explains reported nanodiamond polymorphs. *Sci. Rep.* **2015**, *5*, 18381.
104. Zarubina, V.; Nederlof, C.; van der Linden, B.; Kapteijn, F.; Heeres, H. J.; Makkee, M.; Melián-Cabrera, I., Making coke a more efficient catalyst in the oxidative dehydrogenation of ethylbenzene using wide-pore transitional aluminas. *J. Mol. Catal. A: Chem.* **2014**, *381*, 179-187.
105. Zarubina, V.; Talebi, H.; Nederlof, C.; Kapteijn, F.; Makkee, M.; Melián-Cabrera, I., On the stability of conventional and nano-structured carbon-based catalysts in the oxidative dehydrogenation of ethylbenzene under industrially relevant conditions. *Carbon* **2014**, *77*, 329-340.
106. Mao, S.; Li, B.; Su, D., The first principles studies on the reaction pathway of the oxidative dehydrogenation of ethane on the undoped and doped carbon catalyst. *J. Mater. Chem. A* **2014**, *2* (15).

Table of Contents

